Plasmon-Enhanced Enzyme-Linked Immunosorbent Assay on Large Arrays of Individual Particles Made by Electron Beam Lithography

Si Chen,* Mikael Svedendahl, Tomasz J. Antosiewicz, and Mikael Käll*

Department of Applied Physics, Chalmers University of Technology, 412 96 Göteborg, Sweden

ABSTRACT Ultrasensitive biosensing is one of the main driving forces behind the dynamic research field of plasmonics. We have previously demonstrated that the sensitivity of single nanoparticle plasmon spectroscopy can be greatly enhanced by enzymatic amplification of the refractive index footprint of individual protein molecules, so-called plasmon-enhanced enzyme-linked immunosorbent assay (ELISA). The technique, which is based on generation of an optically dense precipitate catalyzed by horseradish peroxidase at the metal surface, allowed for colorimetric analysis of ultralow molecular surface coverages with a limit of detection approaching the single molecule limit. However, the plasmonic response induced by a single enzyme can be expected to vary for a number of reasons, including inhomogeneous broadening of the sensing properties of individual particles, variation in electric field enhancement over the surface of a single particle and variation in size and morphology of the enzymatic precipitate. In this report, we discuss how such inhomogeneities affect the possibility to quantify the number of molecules bound to a single nanoparticle. The discussion is based on simulations and measurements of large arrays of well-separated gold nanoparticles fabricated by electron beam lithography (EBL). The new data confirms the intrinsic single-molecule sensitivity of the technique but we were not able to clearly resolve the exact number of adsorbed molecules per single particle. The results indicate that the main sources of uncertainty come from variations in sensitivity across the surface of individual particles and between different particles. There is also a considerable uncertainty in the actual precipitate morphology produced by individual enzyme molecules. Possible routes toward further improvements of the methodology are discussed.

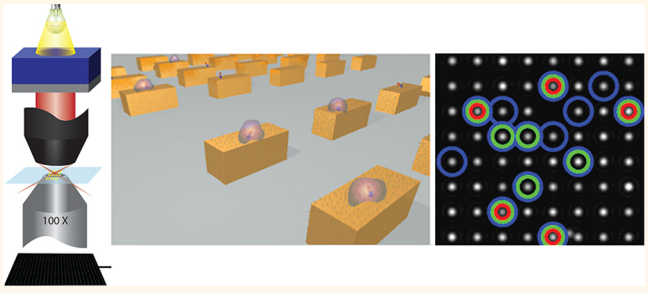

KEYWORDS: LSPR · sensing · enzymatic enhancement · single particle imaging · electron beam lithography

Since the introduction of Surface Plasmon Resonance (SPR) refractive index sensing of gas and biomolecules based on thin metal films almost three decades ago, the interest in plasmon based sensing technology has increased tremendously.[1] The technological advances in conventional SPR sensing have been remarkable, and the commercialization of instruments has greatly expanded the user community. Conventional thin film SPR sensing is now a mature technology that serves as a benchmark for novel optical sensor solutions. The progress in SPR biosensing has been accelerated by progress in several "enabling technologies", in particular development of effective surface chemistry and advanced microfluidic systems. Similarly, enormous recent progress in nanofabrication technologies and computational electrodynamics have resulted in rapid development of novel plasmonic applications, including biosensing based on Localized Surface Plasmon Resonances (LSPR) in metal nanostructures.

The decay length of the evanescent field generated at plasmon resonance ranges from about half the free-space wavelength for propagating plasmons in thin films down to just a few nanometers in "hotspots" around plasmonic nanostructures. Strongly enhanced and localized nanoplasmonic fields are key to surface-enhanced Raman[2] and fluorescence[3,4] spectroscopy, plasmon assisted photolithography,[5] and many other nanophotonic applications of high current interest. In particular, nanometric field

* Address correspondence to si.chen@chalmers.se, mikael.kall@chalmers.se.

Received for review June 27, 2013 and accepted September 11, 2013.

Published online September 11, 2013
10.1021/nn403287a

localization enables refractive index based LSPR detection of molecules attaching at or very close to the metal surface, and this can be utilized for constructing ultrasensitive colorimetric biosensors.[6−8] Compared to classical SPR sensing, which requires a prism or grating to match the momentum of the incident light with that of the propagating plasmon, localized surface plasmons in single nanostructures can be excited and measured in simple extinction or scattering experiments, for example, by using dark-field microspectroscopy.[9,10] Since individual nanoparticles separated by a few characteristic particle diameters from each other effectively behave as isolated sensors, it is possible to perform massively parallel analysis of large particle sensor arrays by hyperspectral imaging.

One of the potentially most rewarding plasmonic applications is to use LSPR sensing for ultrasensitive detection of important disease markers. Recent methodological advances have enabled label-free detection of single protein molecules adsorbing to single LSPR particles, thus demonstrating the intrinsic sensitivity of the technique.[11,12] However, using a single nanoparticle for detecting low concentrations of target molecules is not very efficient since the small reaction surface may lead to a vanishingly small probability of biomolecular binding at equilibrium.[13] A small total surface area also increases the average time it takes until a rare target molecule diffuses to and adsorbs to the sensor.[14] If ultrasensitive detection is the objective, it is therefore necessary to use a single particle *array* as a sensor platform. At low surface coverage, the advantage of single particle resolution is then that the signal from a few positive particles might be resolved in an experiment in which each particle function as an individual sensor while they tend to drown in the many negatives in a standard ensemble averaged measurement. Naturally, the advantage is fully realized only if the signal induced by a single molecule is large enough to be separated from the background. The limit of detection is in principle then determined by the number of individual particles that can be analyzed. This is indeed how Rissin *et al.* managed to reach a detection limit in the subfemtomolar range.[15] In the end, it was the actual number of reaction chambers that could be measured independently that defined the detection limit.

An obvious crucial factor in all sensing methodologies is the magnitude of the signal induced by a single target molecule. We have previously shown that enzymatic signal enhancement based on the well-known ELISA methodology can lead to a dramatic increase of the LSPR peak shift induced by protein adsorption.[16−18] The technique is based on utilizing horse radish peroxidase (HRP) to catalyze a precipitation reaction of its enzyme substrate 3,3′-diaminobenzidine (DAB) on the surface of metal particles in order to increase the "optical mass" associated with protein binding.[16] The peak shift induced by the precipitate was on average almost two orders of magnitude larger than from the HRP protein alone. Using a single particle hyperspectral imaging technique previously described by Bingham *et al.*,[19] we managed to measure extremely low surface coverage of HRP on multiple single particles with an overall detection efficiency in the single molecule range.[16] In this study, we continue our investigations of the "plasmon-enhanced ELISA" methodology with the primary objective of understanding sources of inhomogeneous broadening in the single particle response. We use electron beam lithography (EBL) to fabricate large arrays of well-separated single gold particles in order to generate statistically relevant experimental data, and we use electrodynamics simulations in order to understand the response of an individual nanoparticle. We also investigate the morphology of the precipitated DAB clusters using high-resolution microscopy. We conclude by pointing out possible future developments of the methodology.

RESULTS AND DISCUSSION

Figure 1 gives an overview of the experimental setup and methodology. Elastic scattering images and spectra were recorded using dark-field illumination with the nanoparticle arrays placed inside a stainless steel flow cell mounted on an inverted optical microscope. The liquid crystal tunable filter (LCTF, Varispec) is placed between the dark field condenser and the lamp used for plasmon excitation. The LCTF has a 10 nm band-pass, and it covers a spectral range from 650 to 1100 nm. Using this measurement methodology, we recorded individual particle spectra from arrays that contained 700 individual particles simultaneously. For comparison, we also recorded nanoparticle spectra using standard dark-field spectroscopy and a fiber-coupled spectrometer (B&W Tek Prime X). A schematic of the reactions used for the biosensing experiments is shown in Figure 1b. The biotinylated nanorods are placed in the flow cell on the microscope stage, and a certain concentration of streptavidin conjugated with HRP (SA-HRP) is introduced. After incubation for 1 h, the flow cell is rinsed with PBS buffer. The precipitation reaction is initiated by introducing 1 mM DAB (Thermo Scientific) and 1 mM H_2O_2 into the flow cell. The reaction is then allowed to proceed for 6 min, after which excess DAB is removed by thorough PBS rinsing. Nanoparticle spectra were measured just before the introduction of DAB and just after PBS rinsing. The negative control is performed by precipitation of 1 mM DAB and 1 mM H_2O_2 without SA-HRP incubation. Nonspecific adsorption is quantified by adsorbing 2 pM SA-HRP to a 100% thiol-PEG functionalized gold particle surface and thereafter performing the precipitation reaction.

Figure 2a shows two examples of scattering spectra from individual single particles recorded using

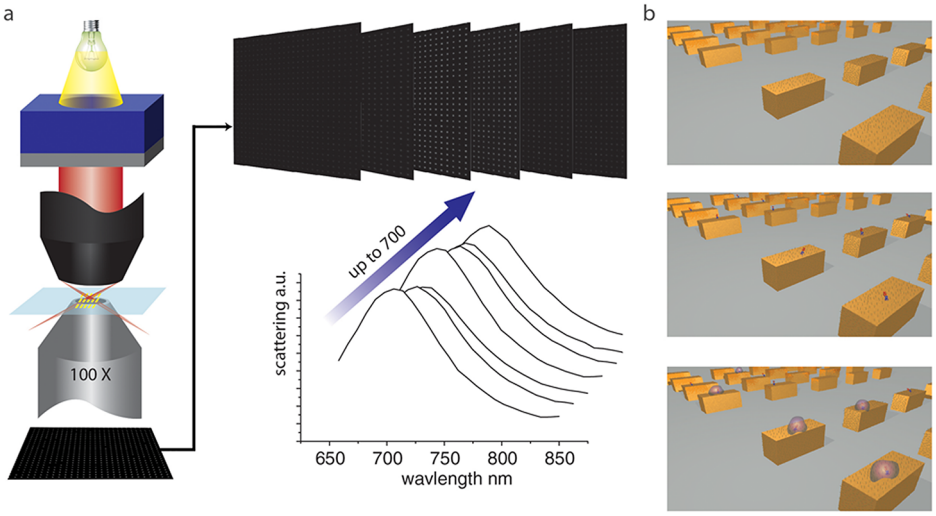

Figure 1. (a) Schematic of the setup and the measurement procedure. The particle array is illuminated through a dark-field (DF) condenser by white light from a xenon lamp that has been band-pass filtered by a liquid crystal tunable filter (LCTF). Elastically scattered light from single particles in the array is collected by a 100× oil immersion objective and projected on a CCD chip. Images are collected for a number of wavelengths, and the complete image stack is used to reconstruct spectra for each individual particle in the array. (b) Schematic of SA-HRP induced enzymatic enhancement. The particle array is first functionalized with thiolated PEG with 1% biotin, and SA-HRP is then allowed to bind, after which the precipitation reaction is started by introducing the enzyme substrate DAB. Precipitates formed on the metal surface cause a shift in the scattering spectrum due to the refractive index sensitivity of the particle plasmons.

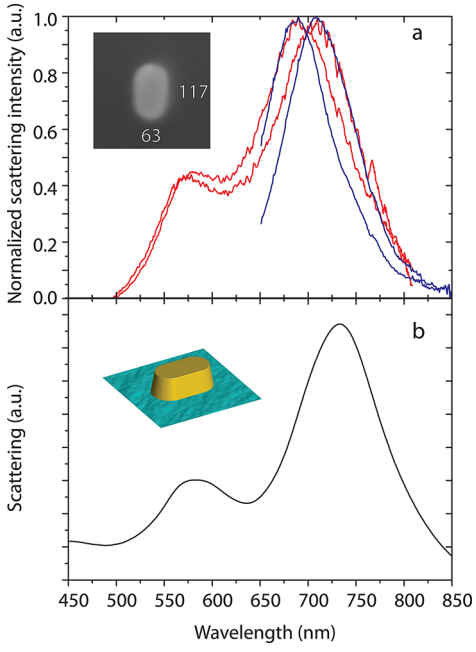

Figure 2. (a) Scattering spectra of two individual particles measured by LCTF imaging (blue lines) and a fiber coupled spectrometer (red lines). The inset shows a SEM image of a single nanorod. (b) FDTD simulation of the elastic scattering spectrum of a nanorod. The inset shows a picture of the particle shape used for the simulation.

unpolarized white light. The particles support two orthogonal in-plane dipolar plasmon oscillations with dipole moments parallel and perpendicular to the long axis of the particle, respectively. The long-axis, or longitudinal mode, is strongly red-shifted compared to the short-axis, or transverse mode, due to depolarization effects caused by the high aspect ratio.[20] We first note that the LCTF spectra compare favorably with ordinary DF spectra measured using the optical spectrometer in terms of signal-to-noise ratio. However, the main difference between the two measurement techniques concerns the polarization sensitivity. Because of the working principle of the LCTF, only one polarization contributes to the image stacks, whereas the fiber-coupled spectrometer records both orthogonal polarizations with equal sensitivity. In the experiments, we therefore aligned the polarization direction transmitted through the LCTF with the long axis of the nanorods so that only the longitudinal plasmon band, which is the most sensitive to refractive index changes, contributed to the spectra. The fiber-coupled spectrometer, on the other hand, measures both transverse and longitudinal plasmons.

Figure 2b shows that our FDTD model, which is built on the dimensions extracted from the SEM image shown in the inset of Figure 2a, captures the spectral properties of the real nanoparticles rather well. The model is based on the assumption that the experimental spectra can be represented by the optical properties of a completely isolated particle. This is a reasonable simplification because the actual interparticle separation (3 μm) is such that near-field interparticle coupling is negligible while diffractive far-field coupling is weak (strong diffractive coupling typically requires that the particle separation is similar to the LSPR excitation wavelength).[10,21]

The spectral differences between the two particles in Figure 2a, which is most likely due to small differences in particle shape, size, and/or degree of crystallinity,

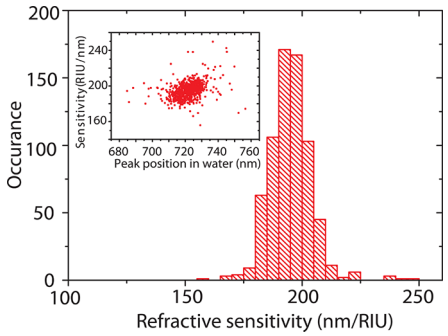

Figure 3. Variation in bulk refractive index sensitivity between different single nanoparticles in an array. The inset shows the same data plotted *versus* the LSPR peak position in water.

illustrate the fact that different particles in an array can be expected have slightly different LSPR properties in general. We investigated to what extent this inhomogeneous broadening effect influences the particle sensing properties by measuring the bulk refractive index sensitivity of the individual particles in an array. The quantification was based on measurements of the LSPR positions in water (n = 1.33) and ethylene glycol (n = 1.49), and the result is summarized as a histogram in Figure 3. The mean of the bulk refractive index sensitivity is 195 nm/RIU (refractive index unit) with a standard deviation of 9 nm/RIU. The inset in Figure 3 shows that there is no clear correlation between the sensitivity and the particles LSPR peak position, although a weak positive slope might be discerned, as can be anticipated from theory and previous studies.

Despite the widespread use of DAB staining for electron microscopy studies of tissues, surprisingly little has been reported about the actual size, morphology and refractive index of precipitates catalyzed by individual HRP enzymes. Moreover, real-time single molecule fluorescence experiments have shown that enzymes possess both static and dynamic inhomogeneity.[22] Although our end-point measurements should average out short-time temporal fluctuations in HRP activity, one can still anticipate inhomogeneous broadening effects due to the individuality of single enzyme molecules. As summarized in Figure 4, we used AFM and TEM imaging to shed some light on the morphology of DAB precipitates and the possible role of enzymatic variation. Figure 4a shows AFM results for HRP on silicon. It is clear that there is a substantial variation in the height of the structures we interpret as DAB precipitates. TEM images after HRP induced precipitation on Formvar show structures with an even higher degree of irregularity (Figure 4c). We used image analysis to extract a characteristic radius for the objects we interpret as DAB precipitates (Figure 4b). The mean height extracted from the AFM measurements was found to be 27 nm, while the characteristic radii extracted from TEM images were 13 nm. The data might thus be interpreted as evidence for more or less

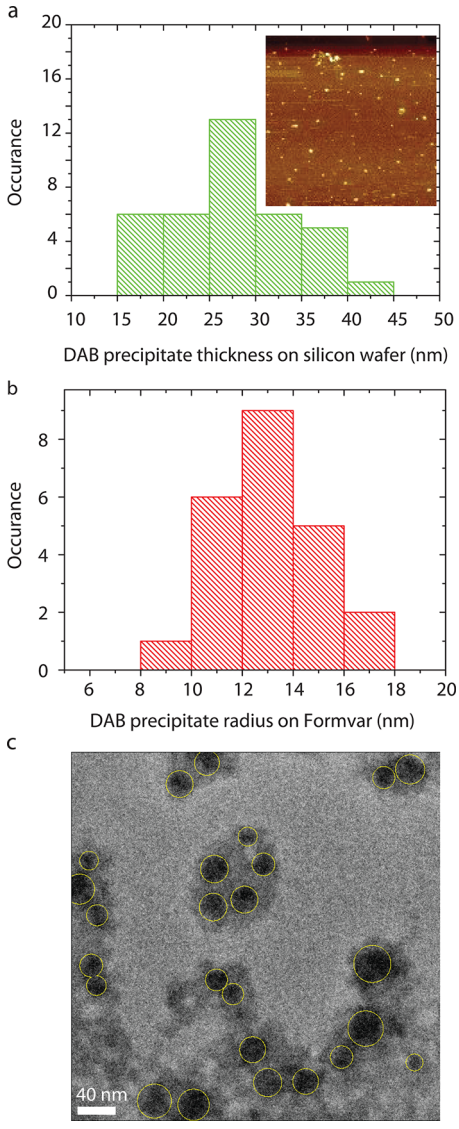

Figure 4. (a) Height distribution of DAB precipitates on a silicon wafer measured by AFM. The inset shows an AFM image of the precipitates. (b) The effective radius distribution of DAB precipitates on a Formvar surface measured by TEM. (c) A TEM image of the DAB precipitates.

spherical precipitates with an average radius of ~13 nm. However, the TEM image also exhibits a film like structure surrounding the dark rounded objects, and it is difficult to rule out that this feature is not the main HRP induced structure. Clearly, a detailed understanding of the physical characteristics of DAB precipitates requires further study.

An additional potentially important source of inhomogeneous broadening is connected to the variation in electromagnetic field-enhancement and RI sensitivity across the surface of an individual nanoparticle. We simulated this effect using FDTD calculations by placing a single dielectric object at different positions around the surface of a nanorod and checking the resulting LSPR peak position compared to a bare nanorod. We modeled the precipitate as a hemisphere with

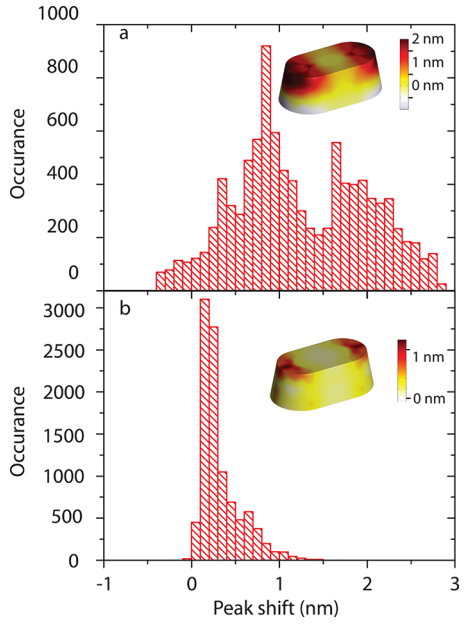

Figure 5. (a) FDTD simulation of the distribution in LSPR peak shifts induced by a single 25 nm radius (a) and a 13 nm radius (b) hemispherical dielectric particle placed at different position on a nanorod excited with incident polarization parallel to the long axis. The insets show a map of the induced peak shifts across the nanorod surface.

n = 1.45. The value for the refractive index is chosen due to the similarity in chemical composition between a protein layer and DAB precipitates. Figure 5a,b shows the resulting peak shift distributions for hemispheres with radii of 25 and 13 nm, respectively. The average peak shifts for these two dimensions are 1.2 and 0.35 nm, respectively. Note that the average shifts do not scale linearly with volume, which would predict a 7 times higher shift for the 25 nm precipitate compared to the 13 nm one. This effect is a direct consequence of the finite LSPR "sensing depth", related to extension of the electromagnetic near-field, which vary across the surface and is of the same order of magnitude as the precipitate radii used in the model. The strongly varying sensitivity is also reflected in the "bimodal" distribution function, which is due to the high sensitivity points near the two tips caused by excitation of the longitudinal plasmon resonance. We also modeled the peak shift induced by thin films of refractive index n = 1.45 (not shown). We found that a 1.5 nm DAB shell homogenously deposited on top of the nanorod produces a 2 nm peak shift.

Figure 6 summarizes experimental plasmon-enhanced ELISA results for HRP concentrations ranging from 50 fM to 2 pM. The average peak-shifts and the observed distributions are similar to our previous report based on gold nanodisks made by hole-mask colloidal lithography. As shown in Figure 6b, the average peak shift varies essentially linearly with concentration at low enzyme concentration. This indicates that the LSPR sensitivity is far from being saturated.

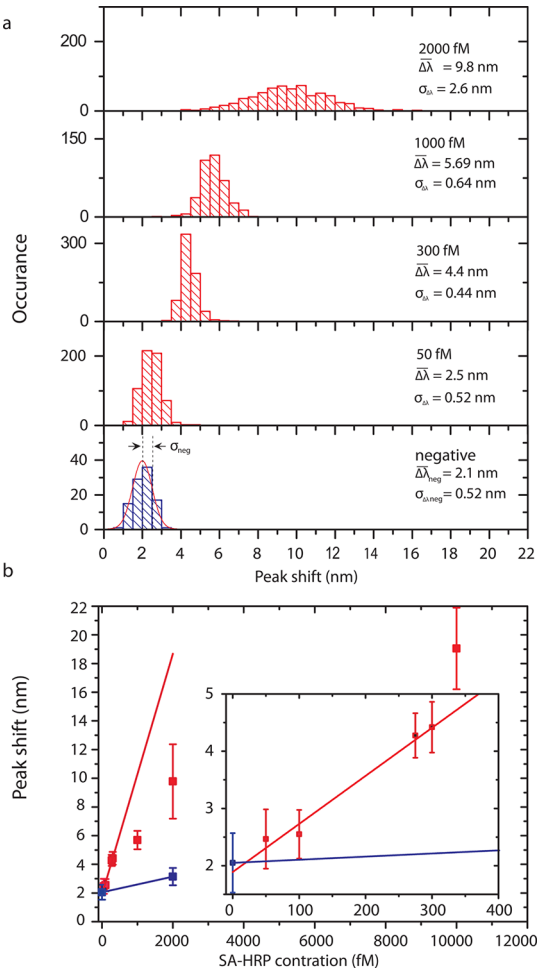

Figure 6. (a) Experimental peak shift distributions for four different SA-HRP concentrations together with the negative control distribution. (b) Average peak shift and standard deviations (shown as error bars) *versus* SA-HRP concentration. The red line is a linear fit to the four lowest concentrations. The blue line is a linear fit to the two negative concentrations. The inset shows a magnification covering the lowest concentrations. The red line crosses the blue line at 20 fM.

Because of the small surface area of a single nanorod and the low concentrations used in the experiments, we expect a very low number of HRP molecules on each of the imaged particles. For low surface coverage Γ, *i.e.*, far from saturation, it can be assumed that the molecular coverage follows the first part of the Langmuir isotherm: $\Gamma(t,c) \propto k_{on} t \Gamma_{max} c$, where k_{on} is the molecular attachment rate, t is the incubation time, Γ_{max} is the maximum surface coverage, and c is the concentration. The surface coverage is then directly proportional to the concentration, which is what is seen experimentally. However, toward the low concentration end of the curve in Figure 6b, one needs to take into account that there is a DAB induced background observed even without HRP present on the sample. The average peak shift of this background is ~2 nm, which yields an array averaged limit of detection (LOD) of the order 20−50 fM for the experimental conditions used.

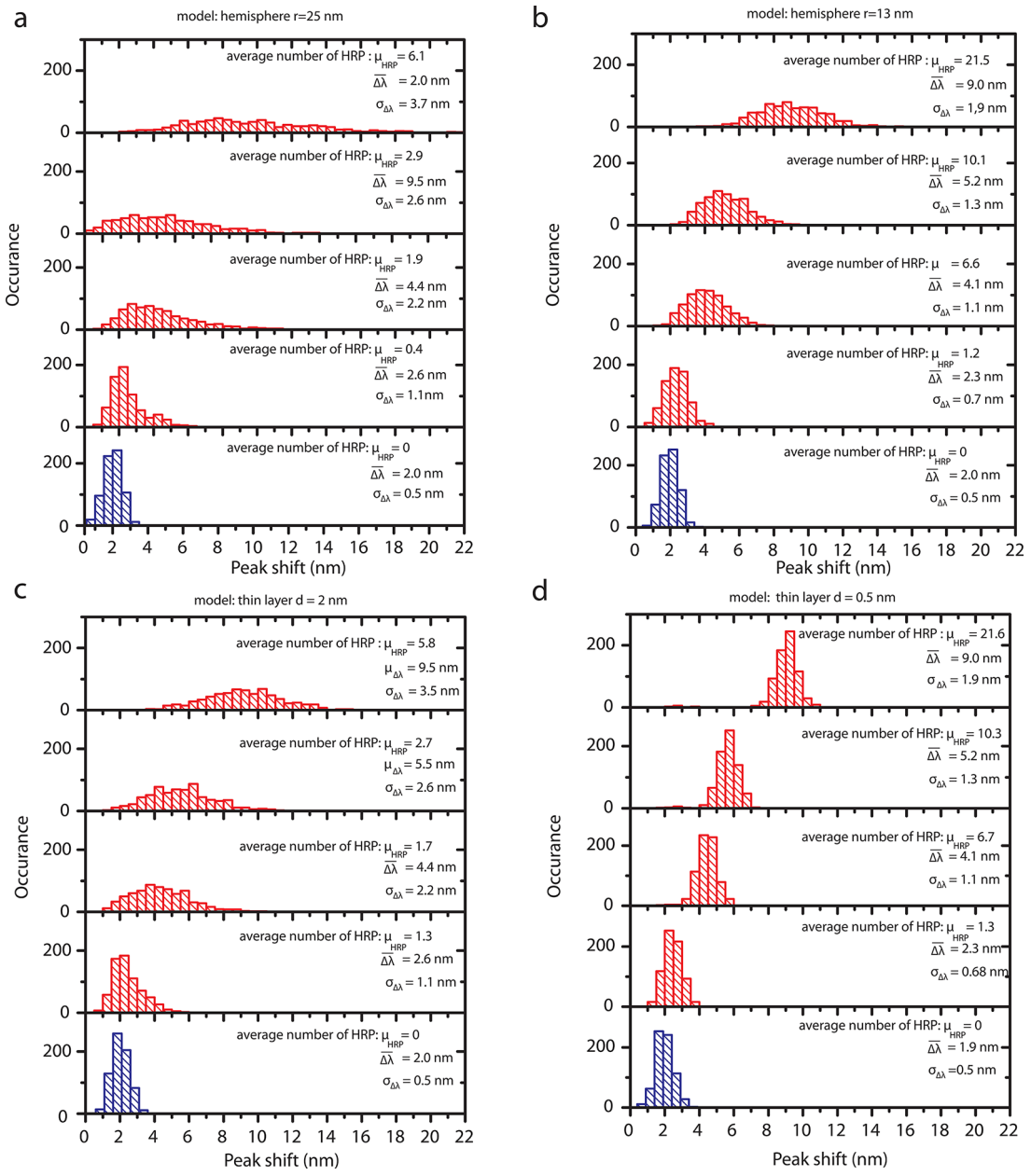

Figure 7. Simulated peak shift distributions for 700 nanorods with varying average number of HRP (μ_{HRP}) molecules per particle. Each particle is assumed to host an integer number of HRP chosen according to a Poisson distribution. The four figures correspond to an assumption that each single HRP generates (a) a hemispherical precipitate with radius 25 nm, (b) a hemispherical precipitate with radius 13 nm, (c) a thin film of thickness 2 nm, or (d) a thin film of thickness 0.5 nm. The $\Delta\lambda$ and $\sigma_{\Delta\lambda}$ values corresponds to the average and standard deviation peak shift, respectively.

The deviation of the experimental data from the linear fit at high concentrations is partly due to saturation, that is, surface crowding that prevents more SA-HRP to bind with maximum efficiency when the amount of SA-HRP starts to accumulate. The high number of HRPs per particle also reduces the precipitation response for each of the HRPs, as we have observed previously.[16]

We simulated experimental data based on the inhomogeneous broadening effects discussed above in order to understand the origin of the peak shift distributions observed and estimate the actual number of HRP molecules contributing to the observed peak shifts. We generated peak shift distributions for 700 different particles, each with a number of HRP molecules chosen according to a Poisson distribution corresponding to a given average number of molecules per particle. Figure 7a,b shows the result when each HRP is assumed to generate a hemispherical precipitate of radius 25 and 13 nm, respectively. The simulation uses the sensitivity distributions in Figure 5, and it is based on the assumption that peak shifts generated by more than one molecule are additive and that precipitates are formed with equal probability over the nanorod surface. For simplicity, we did not include any mutual exclusion or

steric hindrance effects. In addition, we also added a normally distributed background with an average of 2.1 nm and a standard deviation of 0.52 nm, obtained from the blank experiment, to the simulated peak shifts for each of the particles. We also simulated a case when the precipitate is assumed to form a thin sheet with a defined thickness over the particle. As shown in Figure 7c,d, we looked at two cases, *i.e.*, when a single HRP is assumed to form a sheet of thickness 2 or 0.5 nm, respectively. The thickness of a sheet increases with the number of HRP per particle, which is again chosen according to a Poisson distribution, and we let the LSPR sensitivity of each particle vary according to the experimentally observed variation in bulk RI sensitivity shown in Figure 3. Once again a random peak shift picked according to the normally distributed background was added to the peak shift for each of the particles.

The average numbers of molecules per particle μ_{HRP} in the simulation described above were chosen to produce average peak shifts $\Delta\lambda$ similar to the ones found experimentally and the first thing to notice in Figure 7 is that these numbers are indeed very small! In particular, to generate a peak shift of the same magnitude as observed experimentally for the lowest molecular concentration (50 fM), we need to assume one or less than one molecule per particle *irrespective* of the character of the simulated precipitate. This strongly supports the main conclusion in our original report on plasmon-enhanced ELISA, *i.e.*, that the method in principle provides single molecule sensitivity, even though that conclusion was based on a completely different method to determine the number of molecules per particle.[16] The effective k_{on} extracted from the data in Figure 7 varies between 1.5×10^6 and 5.5×10^6 M^{-1} s^{-1}, which is within the broad range of measured k_{on} values previously reported for the streptavidin–biotin biorecognition process.[23−25]

The other clear conclusion from the simulation is that the Poisson distribution in number of molecules per individual particle is washed out due to the inhomogeneous broadening caused by the sensitivity distributions and the background. Thus, it is not possible to clearly demarcate shifts induced by 0, 1, 2, ... molecules per particle *etc.* Further, the similarity between the widths $\sigma_{\Delta\lambda}$ of the distributions in Figure 7b,d and the experimental broadenings speak for a rather low peak shift response from a single HRP. This might indicate that the radius of a precipitate is closer to the 13 nm extracted from the TEM images than the 25 nm radius extracted from AFM measurements. However, it is of course impossible to draw any clear conclusions solely from the distribution simulations and the most likely scenario is perhaps that a HRP can generate both clusters and films of varying dimensions.

Although inhomogeneous broadening presently prevents us from detecting individual single molecule binding events, *i.e.*, to achieve a "digital response", it is interesting to check how many particles in an array exhibit statistically significant peak shifts compared to background for the lowest concentrations. In Figure 8, we have marked those particles in the 50 fM experiment that exhibit peak shifts that differ from the average negative background shift by more than 1.6, 2, and 2.4 σ_{neg}, where σ_{neg} is the standard deviation of the negative distribution and the numbers correspond to the 5, 3, and 1 percentiles in the negative distribution. The numbers of positive particles are 126, 84, and 41, corresponding to 24, 16, and 7% of the total number of particles. To consider a shift measured for a single particle as a real response, $\Delta\lambda$ obviously needs to be well separated from the negative distribution. From the simulation of the sensitivity distribution of the particle, it appears that at least two to three HRPs were required in order to produce a $\Delta\lambda$ large enough to be well separated from the negative distribution. For the experiment with 300 fM, almost all of the particles have made a peak shift larger than 2.4 σ_{neg}.

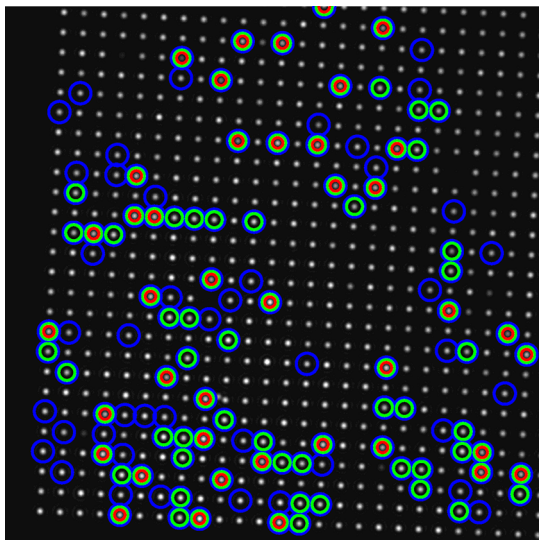

Figure 8. LCTF particle image taken at 650 nm. Particles with a peak shifts larger than 1.6, 2, and 2.4 σ_{neg} are marked with blue, green, and red circles, respectively.

SUMMARY AND CONCLUSIONS

The true advantage of using a large array of single particles for ultrasensitive molecular detection, instead of an ensemble average, is realized only if single binding events can be resolved with high confidence. Ideally, one should be able to observe a bimodal distribution corresponding to 0 or 1 molecules per particle at the lowest concentrations. Thus, to realize the full potential of the present system one would need to decrease the negative background and at the same time increase the magnitude and homogeneity of the peak shift induced by a single HRP molecule.

The background effect is intimately connected to the cause of DAB precipitation in the absence of HRP

activity, which is presently unclear, and it is quite possible that this is the most crucial limiting factor. The response from HRP can potentially be amplified by decreasing the volume of the nanoparticle since the peak shift is inversely proportional to the volume ratio between the plasmonic particle and the dielectric object causing the shift.[26,12] Roughly speaking, by decreasing the volume of the sensor by 50%, one expects to double the peak shift induced by a single precipitate. This could be enough to be able to resolve a single HRP, unless the background increases by the same factor as the true signal. However, decreasing the particle volume also decreases the scattering cross section, which is proportional to volume squared, and the resulting decrease in the amount of light collected from a single particle makes it more difficult to precisely determine the peak shift. On the other hand, the temporal spectral fluctuations that we observe for a blank sample indicate that we are not in the shot-noise limited regime (see Figure S1 in the Supporting Information), so this route toward higher sensitivity appears viable.

There are essentially two avenues toward a more homogeneous LSPR response. Using nanoparticles with a more homogenously distributed field-enhancement would obviously decrease the spread in peak shifts induced by a single HRP, thereby facilitating quantification. On the other hand, a more uniform response implies more rounded nanoparticles, which have smaller refractive index sensitivities than elongated ones.[28] The other route is completely opposite, that is, to use particles with sensitivity "hotspots", such as sharp edges or narrow gaps between particles, which can be completely saturated by a single precipitate while the rest of the particle produces a negligible response. However, for this to work in reality, one probably needs to passivate the insensitive regions of the particle and/or specifically functionalize the hot spot. One also needs to take into account that this route implies a radical decrease of the total nanoparticle area available/used for sensing, which may affect the reaction time needed in an experiment.

In summary, we used spectral imaging with single particle spatial resolution to analyze HRP induced precipitation on an array of 700 gold nanorods fabricated by electron beam lithography. By comparing peakshifts recorded experimentally with electrodynamic simulations, we concluded that the average peak shift observed for the lowest measured HRP concentration corresponds to single molecule sensitivity. However, inhomogeneous broadening and background effects prevented us from counting the exact number of molecules present on each individual nanoparticle.

Altogether, we can conclude that there are no simple solutions to achieve robust LSPR sensing with single molecule resolution for ultrasensitive molecular detection. Further progress will therefore most likely involve optimization and refinement of a range of factors, including measurement strategy, nanoparticle fabrication, surface chemistry, reaction times, enzyme substrate concentrations *etc.* Nevertheless, the fact that the plasmon-enhanced ELISA method as such has an overall sensitivity in the single molecule range indicates that progress is possible and worthwhile.

EXPERIMENTAL METHODS

Sample Fabrication. Arrays of elongated gold nanoparticles were fabricated using electron beam lithography (EBL, Jeol JBX9300FS) on glass substrates. A double resist layer consisting of 130 nm methyl methacrylate (MMA) and 70 nm ZEP520 was used for better lift-off performance, and a 1 nm Cr layer was used to improve the adhesion between gold and the substrate. The dimensions of the particles, as determined by inspection in a scanning electron microscope (SEM), was 60 × 120 nm, the center-to-center distance between particles was 3 μm and the thickness of the evaporated gold film was 40 nm. The parameters were chosen to yield clearly resolvable images of single particles and a long-axis plasmon resonance in the red. All samples were thoroughly cleaned in TL1 (5:1:1 water, 30% hydrogen peroxide and 20% ammonium hydroxide) before use.

Optical Measurements. The nanoparticle array is imaged through a 100× oil-immersion objective with variable numerical aperture on a 1 Mpixel electron-multiplying CCD camera (Andor IXON 885). Array spectra are constructed from 200 images recorded with 1 nm shift of the center wavelength of the LCTF using an exposure time of 1 s for each image. The total measurement time for one image stack is ~4.5 min. To minimize effects of pixel response variation and illumination inhomogeneity, a single particle spectrum is obtained by summing the intensities of the pixels that correspond to that particular particle for each of the measurement wavelengths, subtracting the dark count, and dividing by a reference spectrum recorded from the same camera pixels with the sample removed and the objective aperture opened up.

Surface Functionalization of Nanorods and DAB Characterization. The particle arrays are first immersed in a solution of 99% thiol-PEG (molecular structure S-CH_2-(CH_2-O-CH_2)$_7$-CH_2-OH)$_2$) and 1% thiol-EG-biotin (S-C_2H_4-CO-NH-(CH_2-O-CH_2)$_9$-NH-CO-C_4H_8-Biotin)$_2$ for more than 24 h.[27] We investigated the morphology of DAB precipitates using atomic force microscopy (AFM, Veeco Dimension 3100) and transmission electron microscopy (TEM, FEI Tecnai G2). SA-HRP molecules were physisorbed on the surface of a smooth silicon wafer for AFM studies or on the Formvar surface of a TEM grid. The microscopy substrates were then immersed in a DAB and H_2O_2 reaction mixture for 6 min before rinsing and drying in N_2 gas. The DAB precipitates thus formed were imaged in the AFM operated in tapping mode using a titanium nitrite tip with a ~10 nm curvature and in the TEM operated at 200 kV acceleration voltage.

Electrodynamics Simulations. We simulated the electromagnetic response of the metal nanoparticles by the finite difference time domain (FDTD) method using a commercial software package (Lumerical Solutions, Inc.). The scattering cross section *versus* wavelength for a single nanorod was calculated using a minimum mesh size of 2 nm. The base dimensions of the rod was set to 115 nm (long axis) × 65 nm (short axis), the height was set to 40 nm, and we rounded the shape by using an edge radius of 20 nm and a side wall taper angle of 10°. The particle is placed on a glass substrate (n = 1.45) in water (n = 1.33). We refer to the Supporting

Information for more details of the conditions used to simulate the precipitate induced plasmon shifts.

Conflict of Interest: The authors declare no competing financial interest.

Supporting Information Available: (SI1) Spectral fluctuations and the expected shot noise limitation in the measurements; (SI2) FDTD simulations for a 25 and 13 nm hemispherical dielectric on an elongated particle. This material is available free of charge *via* the Internet at http://pubs.acs.org.

Acknowledgment. The authors thank Junjie Zeng for assisting with the TEM measurements and Andreas Dahlin for valuable comments on the manuscript. This work was supported by the Swedish Research Council (VR) through the Linnaeus Center for Bioinspired Supramolecular Function and Design (SUPRA).

REFERENCES AND NOTES

1. Agio, M.; Alu, A. *Optical Antennas*; Cambridge University Press: Cambridge, 2013.
2. Nie, S.; Emory, S. R. Probing Single Molecules and Single Nanoparticles by Surface-Enhanced Raman Scattering. *Science* **1997**, *275*, 1102–1106.
3. Chen, Y.; Munechika, K.; Ginger, D. S. Dependence of Fluorescence Intensity on the Spectral Overlap between Fluorophores and Plasmon Resonant Single Silver Nanoparticles. *Nano Lett.* **2007**, *7*, 690–696.
4. Wang, S.; Ota, S.; Guo, B.; Ryu, J.; Rhodes, C.; Xiong, Y.; Kalim, S.; Zeng, L.; Chen, Y.; Teitell, M. A.; *et al.* Subcellular Resolution Mapping of Endogenous Cytokine Secretion by Nano-Plasmonic-Resonator Sensor Array. *Nano Lett.* **2011**, *11*, 3431–3434.
5. Ueno, K.; Takabatake, S.; Onishi, K.; Itoh, H.; Nishijima, Y.; Misawa, H. Homogeneous Nano-Patterning Using Plasmon-Assisted Photolithography. *Appl. Phys. Lett.* **2011**, *99*, 011107–011110.
6. Anker, J. N.; Hall, W. P.; Lyandres, O.; Shah, N. C.; Zhao, J.; Van Duyne, R. P. Biosensing with Plasmonic Nanosensors. *Nat. Mater.* **2008**, *7*, 442–453.
7. Brolo, A. G. Plasmonics for Future Biosensors. *Nat. Photonics* **2012**, *6*, 709–713.
8. Chen, S.; Svedendahl, M.; Käll, M.; Gunnarsson, L.; Dmitriev, A. Ultrahigh Sensitivity Made Simple: Nanoplasmonic Label-Free Biosensing with an Extremely Low Limit-of-Detection for Bacterial and Cancer Diagnostics. *Nanotechnology* **2009**, *20*, 434015–434024.
9. Svedendahl, M.; Chen, S.; Dmitriev, A.; Käll, M. Refractometric Sensing Using Propagating *versus* Localized Surface Plasmons: A Direct Comparison. *Nano Lett.* **2009**, *9*, 4428–4433.
10. Jain, P. K.; El-Sayed, M. A. Universal Scaling of Plasmon Coupling in Metal Nanostructures: Extension from Particle Pairs to Nanoshells. *Nano Lett.* **2007**, *7*, 2854–2858.
11. Zijlstra, P.; Paulo, P. M. R.; Orrit, M. Optical Detection of Single Non-Absorbing Molecules Using the Surface Plasmon Resonance of a Gold Nanorod. *Nat. Nanotechnol.* **2012**, *7*, 379–382.
12. Ament, I.; Prasad, J.; Henkel, A.; Schmachtel, S.; Sönnichsen, C. Single Unlabeled Protein Detection on Individual Plasmonic Nanoparticles. *Nano Lett.* **2012**, *12*, 1092–1095.
13. Dahlin, A. B. Size Matters: Problems and Advantages Associated with Highly Miniaturized Sensors. *Sensors* **2012**, *12*, 3018–3036.
14. Sheehan, P. E.; Whitman, L. J. Detection Limits for Nanoscale Biosensors. *Nano Lett.* **2005**, *5*, 803–807.
15. Rissin, D. M.; Kan, C. W.; Campbell, T. G.; Howes, S. C.; Fournier, D. R.; Song, L.; Piech, T.; Patel, P. P.; Chang, L.; Rivnak, A. J.; *et al.* Single-Molecule Enzyme-Linked Immunosorbent Assay Detects Serum Proteins at Subfemtomolar Concentrations. *Nat. Biotechnol.* **2010**, *28*, 595–599.
16. Chen, S.; Svedendahl, M.; Van Duyne, R. P.; Käll, M. Plasmon-Enhanced Colorimetric ELISA with Single Molecule Sensitivity. *Nano Lett.* **2011**, *11*, 1826–1830.
17. Kim, M.-G.; Shin, Y.-B.; Jung, J.-M.; Ro, H.-S.; Chung, B. H. Enhanced Sensitivity of Surface Plasmon Resonance (SPR) Immunoassays Using a Peroxidase-Catalyzed Precipitation Reaction and its Application to a Protein Microarray. *J. Immunol. Methods* **2005**, *297*, 125–132.
18. Lee, T. H.; Lee, S. W.; Jung, J. A.; Ahn, J.; Kim, M. G.; Shin, Y. B. Signal Amplification by Enzymatic Reaction in an Immunosensor Based on Localized Surface Plasmon Resonance (LSPR). *Sensors* **2010**, *10*, 2045–2053.
19. Bingham, J. M.; Willets, K. A.; Shah, N. C.; Andrews, D. Q.; Van Duyne, R. P. Localized Surface Plasmon Resonance Imaging: Simultaneous Single Nanoparticle Spectroscopy and Diffusional Dynamics. *J. Phys. Chem. C* **2009**, *113*, 16839–16842.
20. Bohren, C. F.; Huffman, D. R. *Absorption and Scattering of Light by Small Particles*; Cambridge University Press: Cambridge, 1983.
21. Haynes, C. L.; McFarland, A. D.; Zhao, L.; Van Duyne, R. P.; Schatz, G. C.; Gunnarsson, L.; Prikulis, J.; Kasemo, B.; Käll, M. Nanoparticle Optics: The Importance of Radiative Dipole Coupling in Two-Dimensional Nanoparticle Arrays. *J. Phys. Chem. B* **2003**, *107*, 7337–7342.
22. Xie, X. S.; Lu, H. P. Single-Molecule Enzymology. *J. Biol. Chem.* **1999**, *274*, 15967–15970.
23. Roberta, D. A.; Giuseppe, G.; Giuseppe, S. Real-Time Binding Kinetics Monitored with Surface Plasmon Resonance Imaging in a Diffusion-Free Environment. *Open Spectrosc. J.* **2008**, *2*, 1–9.
24. Gaster, R. S.; Xu, L.; Han, S.-J.; Wilson, R. J.; Hall, D. A.; Osterfeld, S. J.; Yu, H.; Wang, S. X. Quantification of Protein Interactions and Solution Transport Using High-Density GMR Sensor Arrays. *Nat. Nanotechnol.* **2011**, *6*, 314–320.
25. Zhao, S.; Reichert, W. M. Influence of Biotin Lipid Surface Density and Accessibility on Avidin Binding to the Tip of an Optical Fiber Sensor. *Langmuir* **1992**, *8*, 2785–2791.
26. Antosiewicz, T. J.; Apell, S. P.; Claudio, V.; Käll, M. A Simple Model for the Resonance Shift of Localized Plasmons Due to Dielectric Particle Adhesion. *Opt. Express* **2012**, *20*, 524–533.
27. Nilebäck, E.; Feuz, L.; Uddenberg, H.; Valiokas, R.; Svedhem, S. Characterization and Application of a Surface Modification Designed for QCM-D Studies of Biotinylated Biomolecules. *Biosens. Bioelectron.* **2011**, *28*, 407–413.
28. Ueno, K.; Juodkazis, S.; Mino, M.; Mizeikis, V.; Misawa, H. Spectral Sensitivity of Uniform Arrays of Gold Nanorods to Dielectric Enviroment. *J. Phys. Chem. C* **2007**, *11*, 4180–4184.